PHYSICAL REVIEW B **109**, 024111 (2024)

Three charge-ordered phases in bilayered $Pr(Sr_{0.1}Ca_{0.9})_2Mn_2O_7$: From antiferrodistortive to ferrodistortive structures

J. Blasco,[1,2,*] V. Cuartero,[1,3] S. Lafuerza,[1,2] J. L. García-Muñoz,[4] F. Fauth,[5] and G. Subías[1,2]

[1]*Instituto de Nanociencia y Materiales de Aragón (INMA), CSIC-Universidad de Zaragoza, 50009 Zaragoza, Spain*
[2]*Departamento de Física de la Materia Condensada, Universidad de Zaragoza, C/Pedro Cerbuna 12, 50009 Zaragoza, Spain*
[3]*Departamento de Ciencia y Tecnología de Materiales y Fluidos, EINA, Universidad de Zaragoza, C/María de Luna 3, 50018 Zaragoza, Spain*
[4]*Institut de Ciència de Materials de Barcelona, ICMAB-CSIC, Campus UAB, 08193 Bellaterra, Spain*
[5]*CELLS-ALBA Synchrotron, 08290 Cerdanyola del Vallès, Barcelona, Spain*

(Received 22 October 2023; revised 20 December 2023; accepted 22 December 2023; published 26 January 2024)

The structural phase transitions of $Pr(Sr_{0.1}Ca_{0.9})_2Mn_2O_7$ have been studied by synchrotron radiation x-ray powder diffraction. Three different charge order (CO) phases are identified as a function of temperature. The three phases have a checkerboard arrangement of compressed and expanded MnO_6 octahedra in the perovskite bilayers. The structural changes associated with each transition are described in terms of the mode decomposition analysis with respect to the parent tetragonal structure. The high-temperature phase exhibits an orthorhombic symmetry (*Amam*) due to cooperative tilts of the MnO_6 octahedra that can be ascribed to the irreducible representation (irrep) X3−. On cooling, the CO1 phase with *Pbnm* symmetry arises from the condensation of modes belonging to the irrep DT2 together with breathing (X1+) and antiferrodistortive (M5− and Y2) modes. The Mn site is split into two nonequivalent Mn atoms (Mn1 and Mn2) with a small charge segregation, and the asymmetric environment of Mn1 atoms form zigzag chains along the doubled *b* axis. Further cooling leads to the formation of the CO2 phase that comes from a relative change between the directions of previous X3− and DT2 distortions, producing the simultaneous condensation of new DT1 and ferrodistortive GM5− modes. In the CO2 structure (*Am2m* symmetry), Mn2 atoms are split into two nonequivalent sites but with similar oxidation states. Then the checkerboard arrangement between Mn1 and Mn2 atoms is preserved but with a reorientation of the zigzag chains along the *a* axis. At lower temperatures, the CO3 phase arises from a new direction change of irrep X3−, leading to the simultaneous condensation of new secondary modes. Its symmetry is $Pn2_1m$, and the Mn1 site is now split, which leads to a total of four nonequivalent Mn sites in the unit cell. In this phase, more tilts of the MnO_6 octahedra are allowed following the $a^-b^-c^+$ tilt schema.

DOI: 10.1103/PhysRevB.109.024111

I. INTRODUCTION

Manganites have been the subject of intense study in recent years due to their interesting physical properties such as colossal magnetoresistance or high spin polarity that make them very attractive for important technological applications in data storage or spintronics [1–3]. The subtle interplay between lattice, charge, spin, and orbital degrees of freedom in these materials leads to complex and exotic ordered phases which are especially enhanced in half-doped manganites [2]. In these compositions, multiple electronic phases frequently compete. For instance, the ferromagnetic (FM) metallic state competes with several types of charge-orbital-spin ordered phases such as the insulating CE-type magnetic phase in $R_{1/2}A_{1/2}MnO_3$ or $R_{1/2}A_{3/2}MnO_4$ (R = rare earth; A = Ca or Sr) compounds with a checkerboard charge ordering (CO) of an even mixture of formal Mn^{3+} and Mn^{4+} cations [4–6]. This CO state is coupled to an orbital ordering (OO) where occupied e_g orbitals at the Mn^{3+} sites are cooperatively aligned, forming anisotropic orbital stripes [7,8]. This leads to the CE-type order formed by FM zigzag chains of spins that are antiferromagnetic coupled to each neighboring chain [4,9]. It is noteworthy that this model can be considered a first approximation in many systems because, on one side, the effective charge segregation is considerably smaller than the magnitude expected for an ionic model with Mn^{3+}/Mn^{4+} cations, and additionally, the Jahn-Teller distortion associated with the OO is quite small [10,11].

Recently, half-doped manganites have been considered an effective way to achieve improper ferroelectrics [12], where ferroelectricity is driven by either spin ordering, CO, or OO [13]. In this context, the phase diagram of the $Pr(Sr_{1-x}Ca_x)_2Mn_2O_7$ ($0.4 \leqslant x \leqslant 1$) series is a unique and promising case. These compounds present two distinct CO-OO phases which differ in a 90° rotation of the orbital stripes [7]. The high-temperature CO phase (CO1) is centrosymmetric, while the low-temperature CO phase (CO2) is polar. The structural phase transition from CO1 to CO2 occurs at about room temperature for $Pr(Sr_{0.1}Ca_{0.9})_2Mn_2O_7$, which

---

[*] Corresponding author: jbc@unizar.es

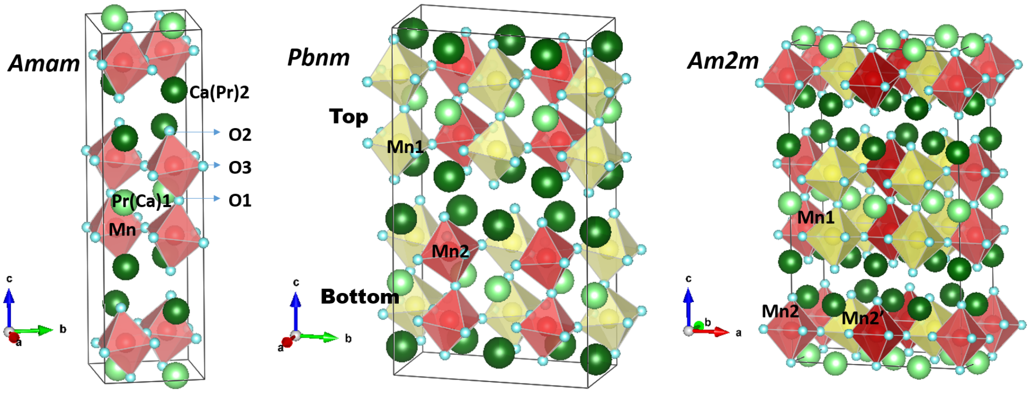

FIG. 1. Crystal structure of (left) the disordered orthorhombic structure, (middle) the CO1 phase, and (right) the CO2 phase for $Pr(Sr_{0.1}Ca_{0.9})_2Mn_2O_7$.

makes it very interesting for technological applications and could profit from the eventual ferroelectric transition coupled to a rotation of the OO direction in memory devices [7,8]. $Pr(Sr_{0.1}Ca_{0.9})_2Mn_2O_7$ belongs to the Ruddlesden-Popper compounds with a layered structure $(AO)(ABO_3)_2$, where two perovskite layers (ABO_3) are separated by a rock-salt layer (AO) along the c axis in this case. The ideal undistorted structure adopts the tetragonal space group $I4/mmm$. Due to cooperative tilts of MnO_6 octahedra, the disordered phase of $Pr(Sr_{0.1}Ca_{0.9})_2Mn_2O_7$ adopts an orthorhombic cell with space group *Amam* which is stable above $T_{CO1} \approx 355$ K (see Fig. 1). At T_{CO1}, there is a phase transition to the CO1 phase with $a_p \times 2b_p \times c_p$ lattice parameters with respect to the previous phase, i.e., the b axis is duplicated. The zigzag chains are propagated along the b axis, while the orbital stripes are parallel to the a axis [7,14]. The resulting space group is centrosymmetric (*Pbnm*) as can be seen in Fig. 1. At $T_{CO2} \approx 295$ K, a new transition gives rise to the CO2 phase. This second CO phase is characterized by a 90° rotation of the orbital stripes, and now the zigzag chains are propagated along the a axis [7,14]. The new cell is $2a_p \times b_p \times c_p$ with polar space group *Am*2*m* (see Fig. 1).

Several studies devoted to the characterization of this nonpolar-to-polar transition have been published in the last years, including investigations on how to manipulate this transition, either by varying the temperature or the external pressure [15–17]. Despite all these works, there are still some uncertainties regarding the transition mechanism between these two CO phases. There are several works that report on the coexistence of both phases near room temperature. Some authors explain it in terms of domains with the CO1 phase that nucleates and expands in the matrix of the CO2 phase as the temperature increases. However, an electron microscopy study [18] found $2a_p \times 2b_p \times c_p$ domains, i.e., a and b axes simultaneously duplicated, and suggested that this new ordering could be an intermediate state in the transition between the CO1 and CO2 phases. Closely related to the previous point, the mechanism that induces the appearance of ferroelectricity in the CO2 phase is still a matter of great controversy. Initially, $Pr(Sr_{0.1}Ca_{0.9})_2Mn_2O_7$ was proposed to be an example of an improper ferroelectric induced by the specific CO in the CO2 phase. There is a coupling between the tilts of MnO_6 octahedra and the CO pattern that gives rise to ferrodistortive coupling between neighboring perovskite bilayers in the CO2 phase along the b axis. The coupling is antiferrodistortive in the CO1 phase instead. However, this model has the problem of the small charge disproportionation observed in the CO phases, estimated at 39% of the theoretical value by x-ray diffraction [14] or even negligible by electron microscopy measurements [19]. Furthermore, the CO mechanism as causing improper ferroelectricity has been questioned in related systems such as $LuFe_2O_4$ [20]. Density functional simulations support a main contribution from apical oxygens that are shifted away from the bond center along the b direction in a different magnitude for both Mn sites [21]. This mechanism does not depend on the Mn^{3+}/Mn^{4+} CO pattern but on the occurrence of a cooperative $a^-a^-c^+$ tilt system following Glazer's terminology [22]. Somehow, this model reminds us of the improper hybrid mechanism described in other systems with perovskite layers [23]. The problem, as indicated by Ma *et al.* [19], is that $a^-a^-c^0$ is the tilting mode that agrees with CO2 phase in the $Pr(Sr_{0.1}Ca_{0.9})_2Mn_2O_7$ compound, and the cooperative rotation around the c axis, fundamental for the hybrid mechanism, is absent. Furthermore, the electron microcopy study from Ref. [19] on $Pr(Sr_{0.1}Ca_{0.9})_2Mn_2O_7$ suggests that the main contribution to ferroelectricity is the off-center displacement of Mn atoms, neglecting the contribution from apical oxygens.

To gain insights into these open questions, here, we report on a comprehensive structural study of $Pr(Sr_{0.1}Ca_{0.9})_2Mn_2O_7$ using high-resolution synchrotron radiation x-ray powder diffraction as a function of temperature between 30 and 400 K. Our measurements unveil a detailed mapping of structural properties as a function of temperature, covering the different CO phases in this compound. An advantage of this technique, compared with single-crystal studies, is that complications due to twinning, domain formation, multiple scattering, and self-absorption are strongly minimized. In addition, data analysis in terms of the symmetry-adapted modes method, allows us to identify the distortions related to the different CO phase transitions and therein the most suitable mechanism for the ferroelectric transition as already reported in related systems [24]. In addition, here, we report on a third structural transition in $Pr(Sr_{0.1}Ca_{0.9})_2Mn_2O_7$ at $T_S \approx 95$ K, barely mentioned in previous reports, and the new crystal structure below T_S (also polar) has been thoroughly described.

II. EXPERIMENTAL SECTION

Single crystals of $Pr(Sr_{0.1}Ca_{0.9})_2Mn_2O_7$ were grown using the floating-zone method from polycrystalline precursors. Stoichiometric amounts of dried Pr_6O_{11}, $SrCO_3$, $CaCO_3$, and Mn_2O_3 were mixed, ground, and heated at 1000° C overnight. The resulting powder is reground, pressed into pellets, and sintered at 1350 °C for 24 h in an oxygen gas flow. Thus, the pellets are reground, pressed into rods, and sintered at 1350 °C for another 24 h in the same atmosphere. The rods were mounted in a homemade floating-zone furnace with two semielliptical mirrors [25]. The growth was performed in pure oxygen with a total pressure of 3 bars. The seed and feed bars with diameters of 3.5 mm rotated in opposite directions at 20 rpm with a growth speed of 6 mm/h. The boules are easily cleaved exhibiting flat shinny [0 0 1] surfaces.

Part of the boules were crushed and ground into powder for chemical and structural characterization. The chemical composition of the powders was tested using wavelength dispersive x-ray fluorescence spectrometry (Advant'XP+ model from Thermo-ARL), and the Pr : Sr : Ca : Mn stoichiometry agreed with the expected values within the experimental error (1%). Rietveld analysis of the x-ray patterns was performed using the FULLPROF package program [26] with the symmetry-mode analysis [27]. The input file with the basis modes was obtained from the AMPLIMODES program from Bilbao Crystallographic Server [28]. AMPLIMODES/SYMMODES and ISODISTORT programs [27–29] were used to explore the different distorted structures of the $Pr(Sr_{0.1}Ca_{0.9})_2Mn_2O_7$ compound. The schematic illustrations of the crystal structures were performed with the VESTA program [30].

Synchrotron x-ray powder diffraction (SXRPD) patterns were recorded at the MSPD beam line [31] of the Alba synchrotron (Cerdanyola del Vallès, Spain) using two experimental setups. A high-angular-resolution multianalyzer detector (MAD) coupled to a Dynaflow liquid He cryostat was used to collect SXRPD patterns at selected temperatures (30, 60, 80, 100, 120, 150, and 180 K). The high-throughput position-sensitive detector MYTHEN, which owing to its exceptional dynamic range allows us to detect minor superstructure peaks, was used to continuously collect patterns from 100 to 400 K coupled to an Oxford cryostream to control the temperature. In both cases, the samples were loaded in a borosilicate glass capillary (diameter of 0.7 mm) and kept spinning during data acquisition. A short wavelength $\lambda = 0.4133$ Å was selected to optimize absorption. The value of λ was calibrated using a NIST standard silicon. We have performed two types of measurements; standard patterns to refine unit cells were collected in a heating ramp between 100 and 400 K. The rate was 0.5 K min^{-1}, and the total acquisition time was 6 min/pattern. With this procedure, we collected a pattern every 3 K on average. Secondly, SXRPD patterns with high statistics were measured at low temperature with the MAD setup and at three selected high temperatures (225, 330, and 400 K) with a total acquisition time of 30 min/pattern to perform a full structural characterization.

Magnetic measurements were carried out with a commercial Quantum Design (SQUID) magnetometer. The dc magnetization was measured between 5 and 400 K with an external field of 1 kOe in a single crystal with the magnetic field parallel and perpendicular to the c direction.

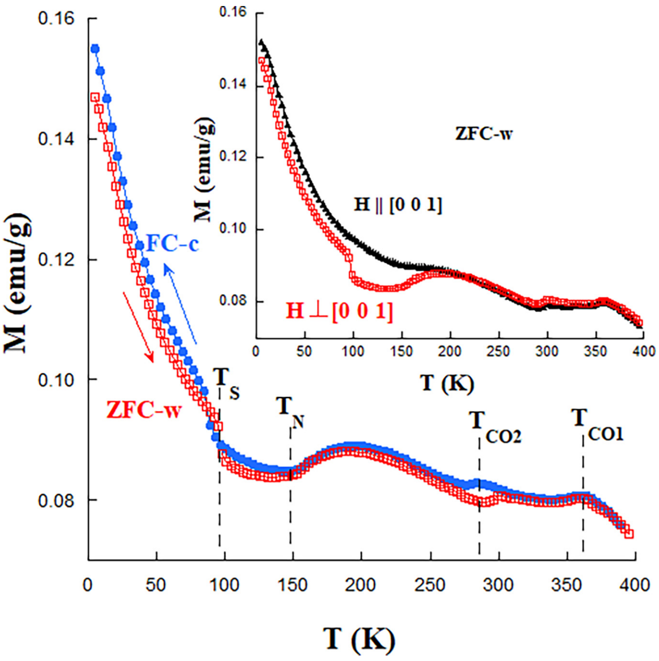

FIG. 2. Temperature dependence of the magnetization under a field of 1 kOe in a warming ramp after zero field cooling (ZFC-w) and in a field cooling ramp (FC-c) for a single crystal of $Pr(Sr_{0.1}Ca_{0.9})_2Mn_2O_7$ with H perpendicular to the c axis or [0 0 1] direction. Inset: Comparison of the ZFC-w measurements for the same crystal in the two indicated orientations.

III. RESULTS, DATA ANALYSIS, AND DISCUSSION

A. Identification of the phase transitions

Figure 2 shows the temperature dependence of the magnetization $M(T)$ for a single-crystal boule of $Pr(Sr_{0.1}Ca_{0.9})_2Mn_2O_7$ with a half-cylindrical shape and with the long flat face along the c direction. This technique has proven to be very sensitive to the different transitions present in $Pr(Sr_{0.1}Ca_{0.9})_2Mn_2O_7$ [8,15]. Here, $M(T)$ was measured in two conditions, heating in a field of 1 kOe after zero field cooling (ZFC-w) and field cooling in the same field (FC-c). The $M(T)$ curves measured with the field perpendicular to the c direction show several anomalies. A local maximum at ≈360 K discloses T_{CO1}. Around room temperature, another anomaly with thermal hysteresis reveals the value of T_{CO2}. This transition is observed ∼300 K in the heating curve but at ∼280 K in FC-c conditions. The observed hysteresis likely suggests a first-order transition for the OO reorientation. At lower temperatures, a broad maximum is observed at $T_{max} = 185$ K, just above the reported long-range magnetic ordering at $T_N \approx 148$ K [8], where our measurements detect a slope change in the $M(T)$ curves and the onset of a small irreversibility between the ZFC and FC conditions. The broad maximum above T_N is observed in related compounds [32], and it was ascribed to either short-range magnetic ordering or quasi-two-dimensional magnetic correlations [33], suggesting that the magnetic transition is developed in

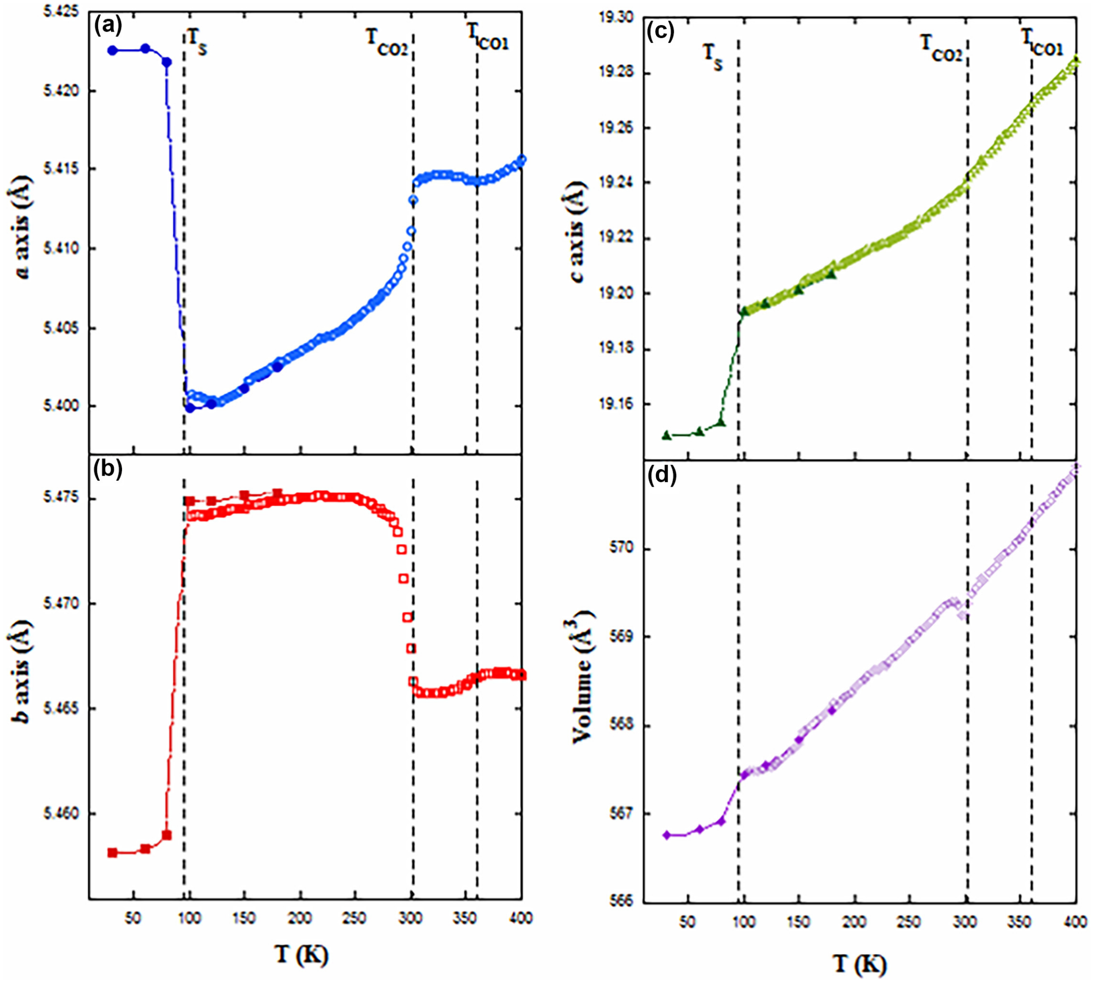

FIG. 3. Temperature dependence of (a)–(c) the lattice parameters and (d) unit cell volume measured with the Mythen detector in a heating ramp from 100 up to 400 K (open symbols) or with the MAD detector at selected points between 30 and 180 K (closed symbols). Dashed lines indicate the temperatures for the structural phase transitions.

two steps. Below T_N, an additional transition $T_S \approx 95$ K is characterized by a small jump in the $M(T)$ curves exhibiting a small hysteresis too. The inset of Fig. 2 proves the magnetic anisotropy between measurement performed parallel and perpendicular to the c direction. The anisotropy begins at the onset of the magnetic correlations, i.e., below $T_{\max}$. For $H \parallel \mathbf{c}$, there is a plateau below $T_{\max}$, and then $M(T)$ increases with decreasing temperature with an upturn point around T_N. For $H \perp \mathbf{c}$, $M(T)$ initially decreases below $T_{\max}$, and then it rises below T_S. Overall, the magnetic properties observed for $Pr(Sr_{0.1}Ca_{0.9})_2Mn_2O_7$ are consistent with previous results from different groups [7,8,34], which confirms the high quality of our single crystals.

Figure 3 shows the temperature dependence of the lattice parameters for $Pr(Sr_{0.1}Ca_{0.9})_2Mn_2O_7$ using the setting of the high-temperature disordered structure *Amam* for the sake of comparison. The main changes are observed in the *ab* plane, as expected from the reorientation of OO within this plane. The *a* and *b* axes follow opposite trends, as can be seen in Figs. 3(a) and 3(b). On cooling, there is a very small contraction of the *b* axis coupled with an expansion of the *a* axis at T_{CO1}. At T_{CO2}, there is a significant and sudden expansion of the *b* axis coupled with a shrinkage of the *a* axis, so the orthorhombic distortion in the *ab* plane increases. The phase transition at T_{CO1} is almost unnoticed on the *c* axis, see Fig. 3(c), while there is a small change in slope at T_{CO2}. Similarly, the evolution of the unit cell volume is neither sensitive to CO1 transition, while a cleft anomaly is noticeable at T_{CO2} [see Fig. 3(d)]. However, the main changes in the lattice parameters occur at T_S, a phase transition barely mentioned in another study on this compound [7]. At this temperature, both *b* and *c* axes compress, while the *a* axis expands with decreasing temperature. The cell volume also shrinks, and the orthorhombic distortion in the *ab* plane diminishes. These changes agree with previous observations in the temperature evolution of some Bragg reflections [35].

Figure 4(a) compares the SXRPD patterns at different temperatures of one of the regions where the superstructure peaks associated with CO appear. At T_{CO1}, superstructure peaks appear following the propagation vector $\mathbf{k}_1 = (0, \frac{1}{2}, 0)$, while below T_{CO2}, superstructure peaks follow the vector $\mathbf{k}_2 = (\frac{1}{2}, 0, 0)$. Figure 4(b) shows the temperature dependence of two representative superstructure peaks between 200 and 400 K. At 200 K, the single superstructure peak follows the $\mathbf{k}_2$ vector. When heating above 263 K, well below T_{CO2}, diffuse scattering appears associated with peaks of the CO1 phase, as

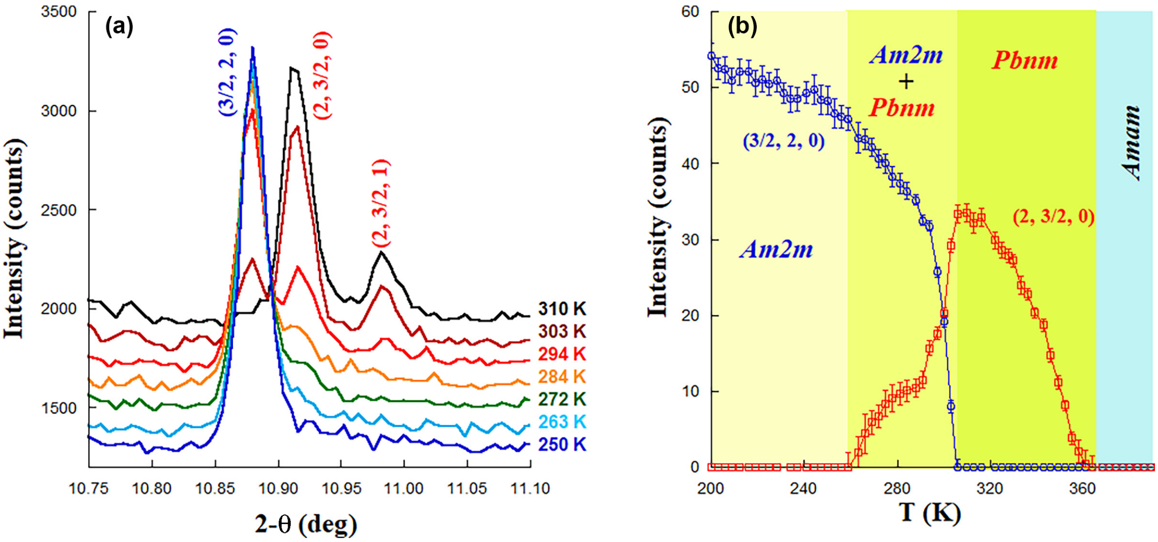

FIG. 4. (a) Detail of the synchrotron x-ray powder diffraction (SXRPD) patterns showing the change of superstructure peaks. (b) Temperature dependence of two selected superstructure peaks.

can be seen in Fig. 4(a), and both CO phases coexist. As the temperature raises, the intensity of the $(2, \frac{3}{2}, 0)$ peak slowly increases while $(\frac{3}{2}, 2, 0)$ intensity decreases, and at $T > 285$ K, this trend is accelerated. At ~306 K, the $(\frac{3}{2}, 2, 0)$ peak vanishes, while the $(2, \frac{3}{2}, 0)$ intensity reaches a maximum. Interestingly, the above temperatures agree quite well with the thermal hysteresis observed in magnetic measurements (see Fig. 1). Further heating leads to an intensity decrease of $(2, \frac{3}{2}, 0)$ peak until it disappears at $T_{\mathrm{CO1}} \approx 360$ K.

The coexistence of CO1 and CO2 phases has been observed previously [17,18,35–37], and some authors have proposed the occurrence of an intermediate phase with two modulations or a propagation vector $\mathbf{k}' = (\frac{1}{2}, \frac{1}{2}, 0)$ [17,18]. Our measurements provide the temperature dependence of both sets of superstructure peaks which is like the one reported in a resonant diffraction study [35] and suggests a nucleation of CO1 domains within the CO2 matrix at the onset of the coexistence region. Then CO1 nuclei grow as temperature increases until CO1 becomes the dominant phase at $T > 300$ K. In this way, we have obtained accurate fits for the SXRPD patterns with a mixture of CO1 and CO2 phases between 263 and 303 K, whose ratio agrees with the ratio of superstructure peaks shown in Fig. 4(b).

B. Symmetry mode analysis for the high-temperature disordered phase

In view of the previous results, summarized in Figs. 2 and 4, we have selected four temperature points to acquire SXRPD patterns with high statistics to accurately determine the different phases present in this sample. To study the disordered phase at high temperature, the patterns were collected at 400 K, well above T_{CO1}. This pattern can be refined in an A-centered orthorhombic cell, see Supplemental Material [38], in agreement with previous reports [7,8]. The refined parameters are summarized in Table I. This cell can be considered a distorted cell of the parent tetragonal lattice with space group *I*4/*mmm* observed in undistorted $(AO)(ABO_3)_2$ compounds [39]. The distortion arises from the cooperative tilting of the MnO_6 octahedra (see Fig. 1) and gives rise to an orthorhombic lattice (*Amam*) with lattice vectors $(1, 1, 0)_T$, $(-1, 1, 0)_T$, and $(0, 0, 1)_T$, where the subscript T refers to the parent tetragonal cell. There are two sites for three A (Pr, Ca, Sr) atoms in this cell (see Fig. 1). We have refined the occupancies of these sites in two steps, keeping the nominal stoichiometry. Firstly, we have refined the Pr/Ca distribution (similar size, different charge) between both sites with the constrain of preserving the atom stoichiometry. Then we have refined the Ca/Sr (same charge, different size) distribution. Convergence is achieved no matter the order of these steps. Our results (see Table I) indicate that Sr is distributed evenly at both sites (≈6.6%), so its occupancy was fixed for the refinements left taken at lower temperatures. On the other side, Pr (≈56%)

TABLE I. Structural parameters of $Pr(Sr_{0.1}Ca_{0.9})_2Mn_2O_7$ obtained from the Rietveld analysis at 400 K. The space group is *Amam* (No. 63, standard setting *Cmcm*). The refined lattice parameters are $a = 5.41580(2)$ Å, $b = 5.46673(2)$ Å, and $c = 19.28596(6)$ Å. The reliability factors are $R_{\mathrm{Bragg}} = 3.64\%$, $R_{\mathrm{wp}} = 6.82\%$, and $\chi^2 = 6.5$.

Atom	Site	*x*	*y*	*z*	Occ.	B_{iso} (Å^2)
Pr1	4*c*	$\frac{3}{4}$	0.7492(4)	0	0.557(1)	0.61(1)
Sr1	4*c*	$\frac{3}{4}$	0.7492(4)	0	0.066	0.61(1)
Ca1	4*c*	$\frac{3}{4}$	0.7492(4)	0	0.377(1)	0.61(1)
Pr2	8*g*	$\frac{3}{4}$	0.2610(3)	0.31610(3)	0.222(1)	0.72(2)
Sr2	8*g*	$\frac{3}{4}$	0.2610(3)	0.31610(3)	0.066	0.72(2)
Ca2	8*g*	$\frac{3}{4}$	0.2610(3)	0.31610(3)	0.712(1)	0.72(2)
Mn	8*g*	$\frac{3}{4}$	0.2521(5)	0.09949(5)	1	0.45(1)
O1	4*c*	$\frac{3}{4}$	0.2978(16)	0	1	1.2(2)
O2	8*g*	$\frac{3}{4}$	0.2085(12)	0.19943(20)	1	1.4(1)
$O3_a$	8*e*	0	0	0.9117(2)	1	0.47(9)
$O3_b$	8*e*	0	0	0.6095(2)	1	0.81(10)

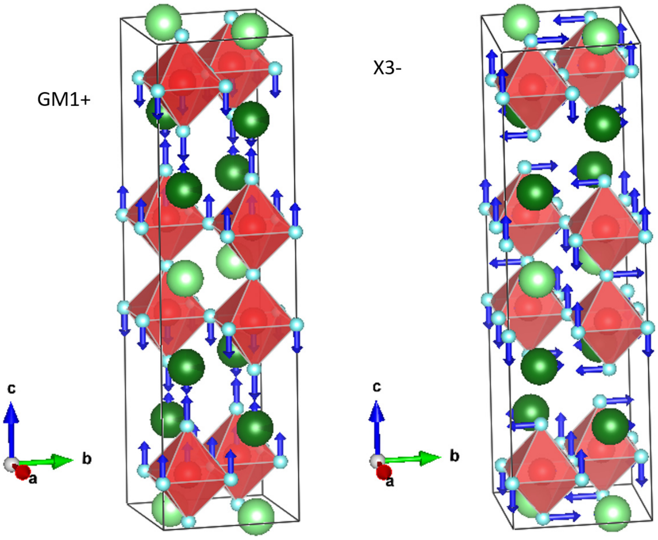

FIG. 5. Representation of the atomic shifts produced by the distortion modes belonging to the irrep GM1+ (left) and X3− (right) in the *Amam* distortion with respect to the parent tetragonal structure.

has a preference for the perovskite site denoted as Pr(Ca)1 in Fig. 1, and Ca (≈71%) is mainly located at the rock-salt layer denoted as the Ca(Pr)2 site in the same figure. This atomic distribution agrees with previous electron microscopy studies [17,19]. In this structure, there are also two positions for the apical oxygens, O1 and O2. The first is shared by the two perovskite units within the bilayer, while the second is also part of the rock-salt layer (see Fig. 1). Finally, the basal oxygen O3 is split into two crystallographic sites in the *Amam* structure, denoted as $O3_a$ and $O3_b$ in Table I.

TABLE II. Comparison of the bond lengths in the MnO_6 octahedra for the different phases of $Pr(Sr_{0.1}Ca_{0.9})_2Mn_2O_7$ studied in this paper.

	Amam	*Pbnm*	*Am2m*	$Pn2_1m$
T (K)	400	330	225	30
Mn1-O1 × 1 (Å)	1.935(1)	1.929(6)	1.926(17)	1.970(12)
Mn1-O2 × 1 (Å)	1.942(4)	1.953(9)	1.934(24)	1.935(37)
Mn1-O3 × 1 (Å)	1.944(2)	1.968(23)	1.858(13)	1.786(20)
Mn1-O3 × 1 (Å)	1.944(2)	1.900(23)	1.914(13)	1.940(20)
Mn1-O3 × 1 (Å)	1.925(2)	2.002(23)	2.015(13)	1.979(20)
Mn1-O3 × 1 (Å)	1.925(2)	1.922(23)	2.031(13)	2.131(20)
Valence (BVS)	3.66(1)	3.58(8)	3.60(7)	3.59(9)
Mn1′-O1 × 1 (Å)	–	–	–	1.941(9)
Mn1′-O2 × 1 (Å)	–	–	–	1.849(37)
Mn1′-O3 × 1 (Å)	–	–	–	1.905(20)
Mn1′-O3 × 1 (Å)	–	–	–	1.998(21)
Mn1′-O3 × 1 (Å)	–	–	–	1.834(20)
Mn1′-O3 × 1 (Å)	–	–	–	2.156(20)
Valence (BVS)	–	–	–	3.69(10)
Mn2-O1 × 1 (Å)	–	1.940(7)	1.934(17)	1.954(11)
Mn2-O2 × 1 (Å)	–	1.895(9)	1.878(24)	1.862(37)
Mn2-O3 × 1 (Å)	–	1.919(22)	1.952(13)	1.948(19)
Mn2-O3 × 1 (Å)	–	1.909(22)	1.952(13)	1.975(19)
Mn2-O3 × 1 (Å)	–	1.918(22)	1.899(13)	1.833(19)
Mn2-O3 × 1 (Å)	–	1.948(22)	1.899(13)	1.917(20)
Valence (BVS)	–	3.82(8)	3.84(7)	3.91(10)
Mn2′-O1 × 1 (Å)	–	–	1.937(17)	1.907(10)
Mn2′-O2 × 1 (Å)	–	–	1.921(24)	1.974(37)
Mn2′-O3 × 1 (Å)	–	–	1.956(13)	1.998(19)
Mn2′-O3 × 1 (Å)	–	–	1.956(13)	2.011(19)
Mn2′-O3 × 1 (Å)	–	–	1.866(13)	1.790(19)
Mn2′-O3 × 1 (Å)	–	–	1.866(13)	1.824(19)
Valence(BVS)	–	–	3.87(7)	3.95(9)

According to the mode formalism [29], this orthorhombic phase can be described as a superposition of distortion modes corresponding to the irreducible representations (irreps) of the undistorted tetragonal cell. Ten distortion modes corresponding to two different irreps are permitted in the distortion from the *I*4/*mmm* structure into the *Amam* one. They are labeled as GM1+(4) and X3−(6). The capital letters refer to the associated *k* points in the first Brillouin zone for the parent tetragonal cell (hereafter, we are using the label GM for the Γ point or DT for the Δ line). The number in parentheses indicates the dimension or number of individual modes for each irrep. Figure 5 shows the atom shifts associated to the distortions of both irreps. Our refinement at 400 K yields absolute amplitudes of 0.24(1) and 0.84(1) Å for GM1+ and X3− distortions, respectively. The atomic displacements associated with the GM1+ distortion are shifts along the *c* axis for all atoms except for O1 and Pr(Ca)1 in the middle of the bilayer, see Fig. 5. The global result of this distortion is an elongation of the perovskite bilayer coupled to a shrinkage of the rock-salt layer along the *c* axis. The main distortion ascribed to X3− is the tilting of MnO_6 octahedra that is responsible for the stabilization of the *Amam* structure. It is composed of a shift of pairs of O3 atoms in opposite directions along the *c* axis coupled to opposite shifts of apical oxygens along the *b* axis, as can be seen in Fig. 5. These displacements lead to out-of-phase tilts of equal magnitude about orthogonal axes in the basal plane of MnO_6 octahedra, giving rise to the $a^-a^-c^0$ tilt system. The rest of the atoms shift much less in opposite directions along the *b* direction, which preserves the inversion symmetry center. Regarding the Mn-O sublattice, the MnO_6 octahedron is quite regular (see Table II), although Mn seems to be a bit overbonded in basis to the value of its valence (+3.66) obtained by the bond valence sum (BVS) method [40], which is slightly higher than the theoretical value (+3.5).

C. Symmetry mode analysis for CO1 phase

To get insights into the CO1 phase, the high-statistical SXRPD pattern was collected at 330 K, a compromise between T_{CO1} and the phase coexistence observed at $T < 306$ K. At this temperature, $(h, k/2, l)_O$ superstructure peaks are clearly noticeable (here, O subscript refers to the *Amam* unit cell), and the pattern can be refined in an orthorhombic cell with a doubled *b* axis with respect to the *Amam* structure. The space group of this phase is *Pbnm*, in agreement with previous results [7,14]. The refined parameters are summarized in Table III, and the fit can be consulted in the Supplemental Material [38]. In this cell, there are two nonequivalent sites for Mn, Pr(Ca), Ca(Pr), O1, and O2 atoms, while there are four inequivalent sites for the basal oxygen O3. The unit cell of this orthorhombic phase can be derived

TABLE III. Structural parameters of $Pr(Sr_{0.1}Ca_{0.9})_2Mn_2O_7$ obtained from the Rietveld analysis at 330 K. The space group is *Pbnm* (No. 62, standard setting *Pnma*). The refined lattice parameters are $a = 5.41459(2)$ Å, $b = 10.93164(3)$ Å, and $c = 19.25521(6)$ Å. The reliability factors are $R_{\text{Bragg}} = 3.90\%$, $R_{\text{wp}} = 6.70\%$, and $\chi^2 = 6.05$.

Atom	Site	x	y	z	Occ.	B_{iso} (Å^2)
$Pr1_a$	4*c*	0.7591(10)	0.0002(6)	$\frac{1}{4}$	0.537(1)	0.32(11)
$Sr1_a$	4*c*	0.7591(10)	0.0002(6)	$\frac{1}{4}$	0.066	0.32(11)
$Ca1_a$	4*c*	0.7591(10)	0.0002(6)	$\frac{1}{4}$	0.397(1)	0.32(11)
$Pr1_b$	4*c*	0.2580(4)	0.2502(6)	$\frac{1}{4}$	0.537(1)	0.49(11)
$Sr1_b$	4*c*	0.2580(4)	0.2502(6)	$\frac{1}{4}$	0.066	0.49(11)
$Ca1_b$	4*c*	0.2580(4)	0.2502(6)	$\frac{1}{4}$	0.397(1)	0.49(11)
$Pr2_a$	8*d*	0.7533(11)	0.0076(5)	0.0659(3)	0.231(1)	0.88(12)
$Sr2_a$	8*d*	0.7533(11)	0.0076(5)	0.0659(3)	0.066	0.88(12)
$Ca2_a$	8*d*	0.7533(11)	0.0076(5)	0.0659(3)	0.703(1)	0.88(12)
$Pr2_b$	8*d*	0.7583(3)	0.2538(5)	0.5661(3)	0.231(1)	0.43(9)
$Sr2_b$	8*d*	0.7583(3)	0.2538(5)	0.5661(3)	0.066	0.43(9)
$Ca2_b$	8*d*	0.7583(3)	0.2538(5)	0.5661(3)	0.703(1)	0.43(9)
Mn1	8*d*	0.7480(18)	0.0017(8)	0.8493(3)	1	0.35(14)
Mn2	8*d*	0.7582(3)	0.2506(8)	0.3496(3)	1	0.36(14)
$O1_a$	4*c*	0.257(3)	−0.025(2)	$\frac{1}{4}$	1	1.0(1)
$O1_b$	4*c*	0.7701(4)	0.277(2)	$\frac{1}{4}$	1	1.0(1)
$O2_a$	8*d*	0.755(2)	−0.0225(15)	0.9498(4)	1	1.0(1)
$O2_b$	8*d*	0.7425(3)	0.2295(15)	0.4472(4)	1	1.02(1)
$O3_a$	8*d*	0.009(4)	0.1262(19)	0.8574(9)	1	0.7(3)
$O3_b$	8*d*	0.003(4)	0.3751(19)	0.3594(9)	1	0.7(3)
$O3_c$	8*d*	0.510(4)	0.1275(19)	0.3365(9)	1	0.6(4)
$O3_d$	8*d*	0.513(4)	0.3734(19)	0.8375(9)	1	1.1(4)

from the undistorted tetragonal cell using the basis vectors $(1, 1, 0)_T$, $(-2, 2, 0)_T$, and $(0, 0, 1)_T$ with a origin shift of $(\frac{1}{4}, \frac{1}{4}, \frac{1}{4})$. According to the mode formalism, the transition from *I*4/*mmm* to *Pbnm* has 38 individual modes grouped in 6 irreps. Table IV lists the irreps present in the different distortions. For each irrep, it gives the particular direction that the modes fulfill within the irrep subspace for the different symmetries and the absolute amplitude (Å) in that space. The amplitudes in Table IV are given for modes normalized within the primitive unit cell of the distorted structure. The number of orthonormal basis symmetry-adapted modes for each distorted phase is commented along the text. Details about this type of mode decomposition analysis can be found in Ref. [28]. In addition, a comparison between our structural study and the one obtained from a single-crystal study [14] can be consulted in the Supplemental Material (Table S1) [38]. In the *Pbnm* structure, we also find distortion modes belonging to the irreps X1+(5), DT2(8), M5−(7), and Y2(8) in addition to the GM1+ and X3− modes described above. Mode decomposition is similar for the structures of both works, showing that the primary mode continues to be the tiltinglike distortion of MnO_6 that belongs to the irrep X3−. The second most important distortion in the *Pbnm* structure corresponds to the irrep DT2 associated with the $(\frac{1}{4}, \frac{1}{4}, 0)$ k point. These modes are responsible for the appearance of the $(h/4, k/4, l)_T$ superstructure peaks associated with the OO. Focusing on basal oxygens, there are three distortion modes with symmetries A_1, B_2, and B_1 (see Fig. 6). These distortions correspond to a tilt of Mn2-O3 bonds around the b axis coupled to a twist distortion of Mn1-O3 bonds (A_1), a Jahn-Teller-like distortion of Mn1-O3 bonds coupled to an asymmetric breathing of Mn2-O3 distances (B_2), and a rotation around the c axis for a $Mn1O_6$ octahedron coupled to an asymmetric scissoring distortion for Mn2-O3 bonds (B_1). The three distortions have significant amplitudes, although the most intense of the three corresponds to the Jahn-Teller-like distortion (B_2), which is the most related to an OO distortion. This distortion is about one-third of that expected for a conventional Jahn-Teller distortion (see Table II) but agrees with the magnitude inferred from resonant soft x-ray diffraction studies [35]. It is also worth noting that this distortion is like that observed in $SmBaMn_2O_6$ [24], which implies that the two nonequivalent Mn sites are anisotropic in the *ab* plane.

Even though the amplitudes of secondary modes from irreps X1+, M5−, and Y2 are significantly smaller than X3− and DT2 ones, they are crucial for the final symmetry of the crystal structure. Focusing on the Mn-O sublattice, the X1+ modes are of particular interest because they lead to the differentiation between $Mn1O_6$ and $Mn2O_6$ octahedra and contribute to the appearance of $(h/2, k/2, l)_T$ superstructure

TABLE IV. Comparison of the mode decomposition (direction and absolute amplitudes) respect to the parent *I*4/*mmm* phase for the four distorted phases found in $Pr(Sr_{0.1}Ca_{0.9})_2Mn_2O_7$.

	Amam (400 K)		*Pbnm* (330 K)		*Am*2*m* (225 K)		$Pn2_1m$ (30 K)	
Irrep	Dir.	Amp. (Å)	Dir.	Amp. (Å)	Dir.	Amp. (Å)	Dir.	Amp. (Å)
GM1+	(a)	0.24(1)	(a)	0.356(3)	(a)	0.25(1)	(a)	0.28(1)
GM5−	–	–	–	–	(a, $-a$)	0.09(4)	(a, $-a$)	0.70(8)
DT1	–	–	–	–	(a,0;0,0)	0.17(1)	(0,a;0,0)	0.66(6)
DT2	–	–	(0, 0; a, 0)	0.43(4)	(0, a; 0, 0)	0.44(2)	(a,0;0,0)	0.64(4)
X1+	–	–	(0; a)	0.14(3)	(a;0)	0.08(4)	(a;0)	0.19(7)
X2+	–	–	–	–	–	–	(0; a)	0.09(10)
X3−	(a;0)	0.84(1)	(a;0)	1.71(2)	(a;0)	1.24(1)	(a; b)	1.76(3)
M2+	–	–	–	–	–	–	(a)	0.10(6)
M5−	–	–	(a;0)	0.13(5)	–	–	(0; a)	0.23(8)
Y1	–	–	–	–	–	–	(0, 0; a, 0)	0.35(9)
Y2	–	–	(0,a;0,0)	0.18(4)	–	–	(0,0;0,a)	0.45(5)

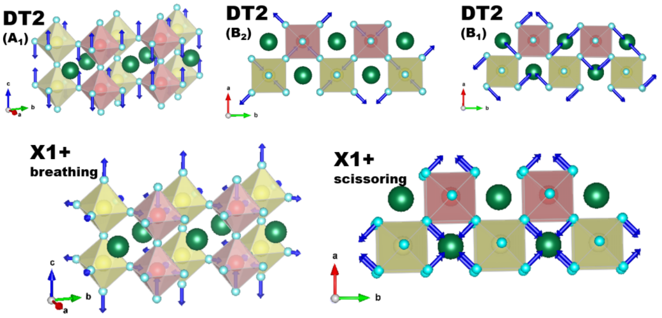

FIG. 6. Representation of the atomic shifts produced by the distortion modes belonging to the irreps DT2 (top) and X1+ in the oxygens of a bilayer of the *Pbnm* distortion.

peaks associated with a CO. Figure 6 shows the two modes presented in this distortion. There is a breathing mode which produces a shortening of the Mn2-O3 and Mn2-O2 distances, while the Mn1-O3 and Mn1-O2 bonds are lengthened, but it does not act on the apical oxygen O1. This mode competes with a symmetric scissoring mode that operates in different directions for the basal oxygens of both octahedra (see Fig. 6). Our refinement reveals a small charge segregation between both Mn sites as inferred from BVS analysis (see Table II), which yields values of +3.58 and +3.82 for Mn1 and Mn2, respectively. The charge segregation of 0.24 e^- is somewhat smaller than the one reported from a single-crystal study [14], but it agrees with the ones found in related manganites [10,11]. The result is a checkerboard arrangement of a bit expanded (Mn1) and compressed (Mn2) MnO_6 octahedra in the perovskite bilayer (see Fig. 1).

The space of Y2 distortion has eight dimensions, while the M5− distortion subspace is seven dimensional. The individual modes belonging to both irreps have one characteristic in common: The distortion directions change between neighboring bilayers (top and bottom in Fig. 1), leading to antiferrodistortive distortions of the atoms in the unit cell that preserve the inversion center. The individual modes can be consulted in the Supplemental Material [38].

D. Symmetry mode analysis for CO$_2$ phase

The $(h, k/2, l)_O$ superstructure peaks have vanished at 225 K, and they have been replaced by $(h/2, k, l)_O$ reflections. The space group of the CO2 phase is *Am*2*m* with a double *a* axis, in agreement with previous reports [7,14]. The refined parameters are summarized in Table V, and the quality of the fit can be seen in the Supplemental Material [38]. In the *Am*2*m* unit cell, there are three inequivalent sites for Pr(Ca), Ca(Pr), O1, O2, and Mn atoms (compressed octahedra are split), while there are still four inequivalent sites for the O3 atoms. Its structure can be derived from the parent tetragonal cell using the vectors $(2, 2, 0)_T$, $(-1, 1, 0)_T$, and $(0, 0, 1)_T$ without origin shift. The mode decomposition of this distortion is shown in Table IV compared with the other distortions found in this sample. This mode decomposition is also compared with a previous structural refinement from Ref. [14] in the Supplemental Material (Table S2) [38] showing similar features. There are 41 distortion modes corresponding to 6 irreps (see Table V) in the transition from *I*4/*mmm* to *Am*2*m*.

TABLE V. Structural parameters of $Pr(Sr_{0.1}Ca_{0.9})_2Mn_2O_7$ obtained from the Rietveld analysis at 225 K. The space group is *Am*2*m* (No. 38, standard setting *Amm*2). The refined lattice parameters are $a = 10.80877(3)$ Å, $b = 5.47501(1)$ Å, and $c = 19.21826(6)$ Å. The reliability factors are $R_{\mathrm{Bragg}} = 3.75\%$, $R_{\mathrm{wp}} = 6.0\%$, and $\chi^2 = 4.25$.

Atom	Site	x	y	z	Occ.	B_{iso} (Å^2)
$\mathrm{Pr1_a}$	2*a*	0	0.4982(16)	0	0.557(1)	0.38(13)
$\mathrm{Sr1_a}$	2*a*	0	0.4982(16)	0	0.066	0.38(13)
$\mathrm{Ca1_a}$	2*a*	0	0.4982(16)	0	0.377(1)	0.38(13)
$\mathrm{Pr1_b}$	4*c*	0.2553(6)	0.0066(14)	0	0.557(1)	0.42(8)
$\mathrm{Sr1_b}$	4*c*	0.2553(6)	0.0066(14)	0	0.066	0.42(8)
$\mathrm{Ca1_b}$	4*c*	0.2553(6)	0.0066(14)	0	0.377(1)	0.42(8)
$\mathrm{Pr1_c}$	2*b*	0.5	0.5171(16)	0	0.557(1)	0.34(9)
$\mathrm{Sr1_c}$	2*b*	0.5	0.5171(16)	0	0.066	0.34(9)
$\mathrm{Ca1_c}$	2*b*	0.5	0.5171(16)	0	0.377(1)	0.34(9)
$\mathrm{Pr2_a}$	4*d*	0	0.4751(5)	0.1843(5)	0.221(1)	0.43(10)
$\mathrm{Sr2_a}$	4*d*	0	0.4751(5)	0.1843(5)	0.066	0.43(10)
$\mathrm{Ca2_a}$	4*d*	0	0.4751(5)	0.1843(5)	0.712(1)	0.43(10)
$\mathrm{Pr2_b}$	8*f*	0.2494(4)	0.0113(3)	0.1837(4)	0.221(1)	0.35(6)
$\mathrm{Sr2_b}$	8*f*	0.2494(4)	0.0113(3)	0.1837(4)	0.066	0.35(6)
$\mathrm{Ca2_b}$	8*f*	0.2494(4)	0.0113(3)	0.1837(4)	0.712(1)	0.35(6)
$\mathrm{Pr2_c}$	4*e*	0.5	0.5024(5)	0.1844(5)	0.221(1)	0.72(12)
$\mathrm{Sr2_c}$	4*e*	0.5	0.5024(5)	0.1844(5)	0.066	0.72(12)
$\mathrm{Ca2_c}$	4*e*	0.5	0.5024(5)	0.1844(5)	0.712(1)	0.72(12)
Mn1	8*f*	0.2492(8)	0.0076(11)	0.4007(9)	1	0.36(12)
Mn2	4*d*	0	0.4928(12)	0.4007(9)	1	0.14(18)
Mn2′	4*e*	0.5	0.5123(12)	0.4000(9)	1	0.26(13)
$\mathrm{O1_a}$	2*a*	0	−0.0651(20)	0	1	0.97(13)
$\mathrm{O1_b}$	4*c*	0.2444(6)	0.5547(19)	0	1	0.97(13)
$\mathrm{O1_c}$	2*b*	0.5	−0.0325(20)	0	1	0.97(13)
$\mathrm{O2_a}$	4*d*	0	0.542(3)	0.3040(9)	1	0.59(7)
$\mathrm{O2_b}$	8*f*	0.2517(5)	−0.0406(13)	0.3010(9)	1	0.59(7)
$\mathrm{O2_c}$	4*e*	0.5	0.550(3)	0.3006(9)	1	0.59(7)
$\mathrm{O3_a}$	8*f*	0.1248(12)	0.238(2)	0.3897(4)	1	0.80(6)
$\mathrm{O3_b}$	8*f*	0.3762(12)	0.768(2)	0.4141(4)	1	0.80(6)
$\mathrm{O3_c}$	8*f*	0.6237(12)	0.276(2)	0.3927(4)	1	0.80(6)
$\mathrm{O3_d}$	8*f*	0.8777(12)	0.738(2)	0.4130(4)	1	0.80(6)

When comparing the active modes present in the CO1 and CO2 phases (see Table IV), it is observed that those belonging to the irreps GM1+, DT2, X1+, and X3− are alike for the two symmetries. The primary mode is still the distortion associated with the irrep X3−, particularly the cooperative tilts of MnO_6 octahedra around the *a* axis. As in the CO1 phase, the most important secondary order parameter of the CO2 phase is the irrep DT2. It is noteworthy that the order parameter direction for DT2 has changed for the CO2 phase with respect to the CO1 phase (see Table IV). This leads to the direction change in the alignment of the CO stripes from the *a* to the *b* axis. In addition, the coupling of the irrep DT2 with X3− gives rise to a polar structure. It is important to indicate that the same polar structure is obtained if the direction of the DT2 distortion is maintained and that of X3− is changed. This indicates that the symmetry of the resulting structure (polar or not) depends on the coupling of the two main distortions (X3− and DT2) and the relative directions of their distortions. Accordingly, the irreps Y2 and M5− with antiferrodistortive distortions are no longer active in the

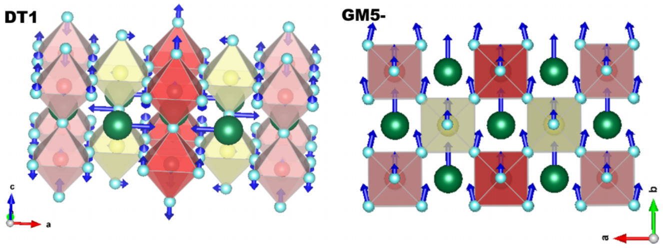

FIG. 7. Schema of the atomic shifts produced by the distortions DT1 (left) and GM5− (right) present in the *Am*2*m* structure of $Pr(Sr_{0.1}Ca_{0.9})_2Mn_2O_7$.

*Am*2*m* symmetry, and they are replaced by new secondary distortions associated with the irreps DT1 and GM5−. The latter allows a ferroelectric distortion along the *b* axis, and it can be considered an induced side effect of the coupling of X3− and DT2 distortions with the appropriate directions. Our refinement reveals that the Jahn-Teller-like distortion mainly affects the expanded Mn1 site which occupies the 8*f* Wyckoff site (see Tables II and V). BVS calculations yield a value of 3.60(7), very similar to the one found for Mn1 in the *Pbnm* structure. The Mn1 is a bit overbonded with an oxidation state quite far from a conventional Mn^{3+} cation. The other two Mn atoms, Mn2 and Mn2′, which are even more overbonded, are located at the 4*d* and 4*e* sites, and the valences obtained from the BVS method are 3.84(7) and 3.87(7), respectively. Therefore, both CO1 and CO2 phases have a similar small charge segregation between Mn sites, and the checkerboard pattern in the *ab* plane is preserved in this transition [7,14].

Figure 7 shows the polarization vector of the secondary distortions DT1 and GM5− focused on a single bilayer. The resulting distortion arising from irrep DT1 can be viewed as a tilt around the *b* axis for the $Mn1O_6$ octahedron coupled to vertical shifts (along the *c* axis) for basal and apical oxygens of $Mn2O_6$ and $Mn2'O_6$ octahedrons in opposite directions. Mn2 and Mn2′ are also slightly displaced along the *c* axis but in opposite directions to their basal oxygens and therefore become two nonequivalent sites. In addition to the shifts along the *c* axis, basal oxygens combine a minor contribution of scissoring and breathing modes along the *ab* plane. Finally, Pr(Ca)1 atoms are slightly displaced along the *a* axis in the opposite direction to the apical oxygen of the $Mn1O_6$ octahedron and of Mn2 itself. Regarding GM5−, we have fixed to zero the individual mode for the Ca(Pr)2 atom to set a reference. The resulting ferroelectric distortion affects all other atoms moving along the *b* axis in the same direction and can be seen in Fig. 7. The displacement of the Mn atoms is identical in this direction, indicating the absence of Mn-Mn dimerization, in agreement with a recent microscopy study [19], although in our case, there is also a significant contribution from Pr(Ca)1 atoms. Two individual modes (asymmetric scissoring and breathing) are acting on O3 atoms along the *ab* plane, which leads to two shorter Mn-O3 distances in a similar way to what it is observed in the orthorhombic phase of $BaTiO_3$ [29].

Simultaneous condensation of modes with different symmetries have already been observed in related systems [41], and it is the base for the hybrid mechanism that produces improper ferroelectrics in several structures with perovskite layers [23,42]. Such a mechanism was proposed for this compound without the need of significant CO [21]. However, this mechanism is reported for bilayer compounds with the $a^-a^-c^+$ tilt system which is not the case for CO2 phase. Ma *et al.* [19] proposed that ferroelectricity can take place in the CO2 phase by the coupling of a single tilt mode (belonging to the irrep X3−) with an OO ordering (belonging to DT2). However, both tilt and Jahn-Teller-like distortion ascribed to the OO take place in the nonpolar CO1 phase too, so that its occurrence is not a sufficient condition. Therefore, it is necessary that both distortions occur in a certain direction.

E. Crystal structure below T_S: Symmetry mode analysis for CO_3 phase

Below $T_S \approx 95$ K, there are sudden changes in the lattice parameters (see Fig. 3) which are the sign for a new phase transition, also reflected in the macroscopic magnetic properties (see Fig. 2). Hereafter, we denote the phase below T_S as CO3. Along with this change in the unit cell, the SXRPD patterns show new diffraction peaks with the same unit cell as CO2 that is no longer A centered (see Fig. 8). These peaks are weak and broad, suggesting a smaller coherence length of the distortion responsible for this new phase transition. This transition was previously observed in two reports. Tokunaga *et al.* [7] reported a structural transition from *Am*2*m* to a monoclinic phase with a rotation of the MnO_6 octahedra. Beale *et al.* [35] detected the sudden change in the lattice parameters and a reduction of the apparent orthorhombic distortion, but they did not observe any monoclinic distortion. In our SXRPD patterns using the MAD detector with a typical angular resolution of 0.005° in full width at half maximum of a diffraction peak [31], no monoclinic distortion is observed, in agreement with Beale *et al.* [35]. We have used the tool [28,29] to explore the possible distortions of the *Am*2*m* structure able to account for the new diffraction peaks. The distortions corresponding to the GM point did not give any structure capable of explaining the appearance of these peaks. However, exploring distortions associated with the (0, 1, 0) *Y* point, we found four primitive orthorhombic cells with space groups *Pm*2*m*, *Pn*2*b*, $Pn2_1m$, and $Pm2_1b$ where the new peaks are allowed. As these peaks are scarce and very weak, it is therefore very challenging to unambiguously determine the actual symmetry of this phase. In fact, the refinement using the *Am*2*m* space group of the CO2 phase gives a good fit except for the aforementioned new peaks. The systematic absences of (0, *k*, 0) and (0, 0, *l*) reflections with all *k* or *l* odd points to either *Pn*2*b* or $Pn2_1m$. The occurrence of (*h*, *k*, 0) reflections with only $h + k =$ even suggests that $Pn2_1m$ (No. 31, standard setting $Pmn2_1$) is the most plausible space group. In addition, this is the simplest model that accounts for the whole pattern. The crystal structure for the CO3 phase can be seen in Fig. 9(a). The Rietveld analysis can be found in the Supplemental Material [38], and the refined data is summarized in the Table VI.

The $Pn2_1m$ structure can be derived from the parent *I*4/*mmm* tetragonal cell using the basis vectors $(2, 2, 0)_T$, $(-1, 1, 0)_T$, and $(0, 0, 1)_T$ with an origin shift of $(\frac{1}{2}, \frac{1}{2}, 0)$. In this structure, there are eight nonequivalent sites for O3 atoms and four nonequivalent sites for the rest of

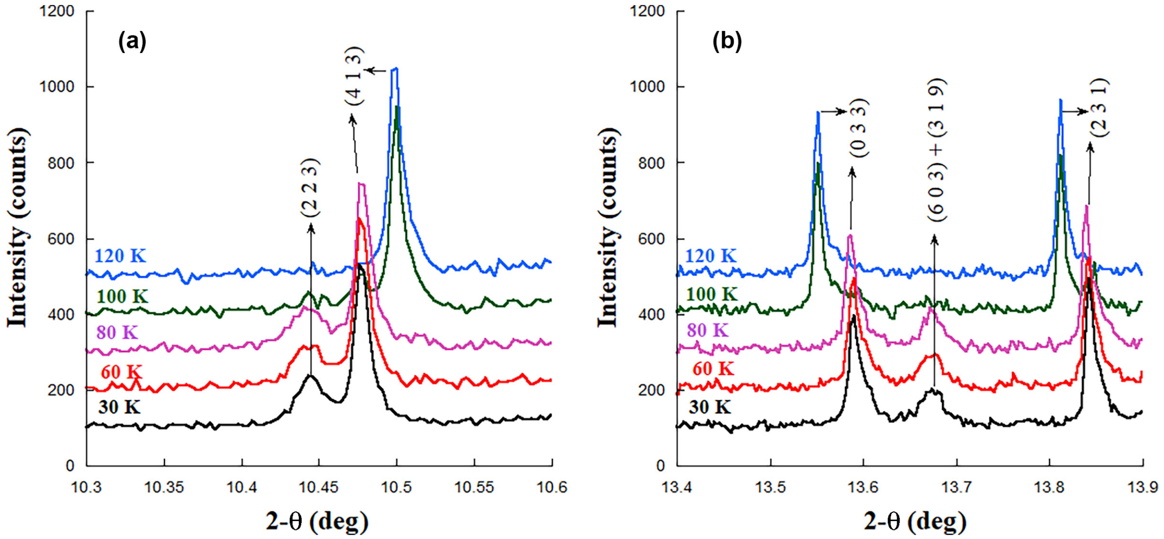

FIG. 8. Detail of the synchrotron x-ray powder diffraction (SXRPD) patterns showing the unit cell changes and the occurrence of new diffraction peaks below $T_S \approx 95$ K for $Pr(Sr_{0.1}Ca_{0.9})_2Mn_2O_7$.

the atoms. Now the Mn1 site (expanded octahedron) is split into two nonequivalent sites, Mn1 and Mn1′. The distortion comprises 76 individual modes grouped into 11 irreps. There are two fundamental differences between the mode decompositions of $Am2m$ and $Pn2_1m$ distortions. First, new modes belonging to irreps Y1(11), Y2(8), X2+(2), M2+(1), and M5−(7) appear in the latest distortion. This implies a total of 29 new degrees of freedom. Secondly, the directions of some irreps change, and this is particularly important for the primary distortion modes belonging to the irrep X3− that is now nine dimensional. Hence, there are three additional individual modes compared with $Am2m$ distortion, and they correspond to a cooperative tilt of the MnO_6 octahedra about the *b* axis that breaks the A-centering symmetry. Figure 9 shows the two types of tilts in this distortion. Figure 9(b) displays the tilt around the *a* axis which is equivalent to the tilt observed in the previous phases above T_S. Figure 9(c) shows the tilt around the *b* axis characteristic of the CO3 phase. The amplitude is different for each tilt, and the resulting distortion can be viewed in Fig. 9(d). Only this variation in the octahedra tilts is enough to suppress the base-centered orthorhombic cell because the isotropic subgroup for the irrep X3− in the $Am2m$ distortion is a base-centered orthorhombic cell (*Cmcm* in standard setting), while the corresponding one for the $Pn2_1m$ one is a primitive cell (*Pnnm*). It is noteworthy that there are additional tilting modes superimposed to this distortion which affect half of the MnO_6 octahedra coupled to twisting modes (irreps DT1 for Mn1-1′ and DT2 for Mn2-2′) that significantly modify the polarization vector of Fig. 9(d). In addition, the $Pn2_1m$ distortion has an active mode belonging to the irrep X2+ that allows the cooperative rotation of O3 atoms in-phase around the *c* axis. Our refinement suggests that the contribution of this mode is very small, but rigorously, the tilt schema for the ground state of $Pr(Sr_{0.1}Ca_{0.9})_2Mn_2O_7$ is no longer $a^-a^-c^0$ but $a^-b^-c^+$ (and almost $a^-b^-c^0$) [22]. It is noteworthy that the $Pn2_1m$ space group was deduced for $a^-b^-c^+$ tilts in bilayer perovskites previously [43]. Accordingly, the trilinear coupling among rotation (X2+), tilt (X3−), and ferroelectric (GM5−) distortions, as observed in related compounds [23,41,42], might be operational below T_S, but it cannot account for the polar structure above T_S.

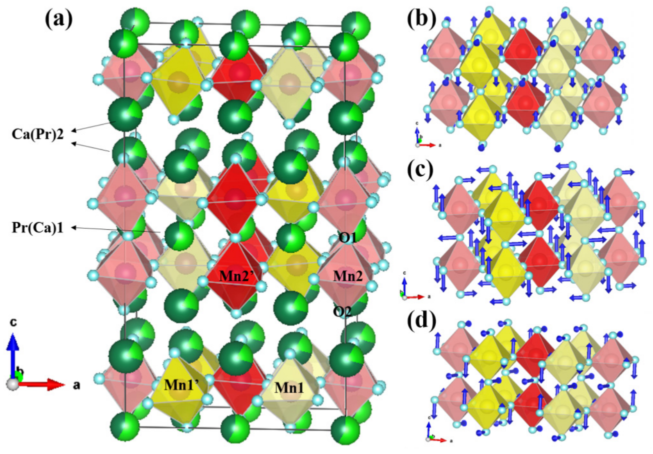

FIG. 9. (a) Crystal structure of the CO3 phase for $Pr(Sr_{0.1}Ca_{0.9})_2Mn_2O_7$. Tilt modes around (b) the *a* axis and (c) the *b* axis for a single bilayer from the irrep X3− in the $Pn2_1m$ distortion. (d) Result of combining the two previous modes.

Bearing in mind that good fits can be obtained using the $Am2m$ model for the patterns measured below T_S, we have performed the fit of these patterns using several constrains to minimize degrees of freedom. First, the individual modes associated with the apical oxygens (O1 and O2) ascribed to tilts (irreps X3−, DT1, and DT2) were constrained to have the same magnitude and opposite directions. Secondly, the individual modes whose standard deviation exceeds the value of its amplitude were neglected. The mode ascribed to the $a^0\, b^0\, c^+$ rotation is in this group, but it is fundamental to determine the tilt schema, so we decided to include it on the refinement. With this procedure, we refined a total of 51

TABLE VI. Structural parameters of $\mathrm{Pr(Sr_{0.1}Ca_{0.9})_2Mn_2O_7}$ obtained from the Rietveld analysis at 30 K. The space group is $Pn2_1m$ with lattice parameters: $a = 10.84510(2)$ Å, $b = 5.45824(1)$ Å, and $c = 19.14861(4)$ Å. $R_{\mathrm{Bragg}} = 5.45\%$, $R_{\mathrm{wp}} = 12.6\%$, and $\chi^2 = 10.1$.

Atom	Site	x	y	z	Occ.	B_{iso} (Å^2)
$\mathrm{Pr1_a}$	2*a*	0.2466(8)	0.4957(16)	0	0.588(1)	0.22(18)
$\mathrm{Sr1_a}$	2*a*	0.2466(8)	0.4975(16)	0	0.066	0.22(18)
$\mathrm{Ca1_a}$	2*a*	0.2466(8)	0.4957(16)	0	0.346(1)	0.22(18)
$\mathrm{Pr1_b}$	2*a*	0.7527(8)	0.4957(16)	0	0.588(1)	0.30(18)
$\mathrm{Sr1_b}$	2*a*	0.7527(8)	0.4957(16)	0	0.066	0.30(18)
$\mathrm{Ca1_b}$	2*a*	0.7527(8)	0.4957(16)	0	0.346(1)	0.30(18)
$\mathrm{Pr1_c}$	2*a*	−0.0025(11)	0.0083(18)	0	0.588(1)	0.30(14)
$\mathrm{Sr1_c}$	2*a*	−0.0025(11)	0.0083(18)	0	0.066	0.30(14)
$\mathrm{Ca1_c}$	2*a*	−0.0025(11)	0.0083(18)	0	0.346(1)	0.30(14)
$\mathrm{Pr1_d}$	2*a*	0.4994(11)	−0.0154(18)	0	0.588(1)	0.13(12)
$\mathrm{Sr1_d}$	2*a*	0.4994(11)	−0.0154(18)	0	0.066	0.13(12)
$\mathrm{Ca1_d}$	2*a*	0.4994(11)	−0.0154(18)	0	0.346(1)	0.13(12)
$\mathrm{Pr2_a}$	4*b*	0.7514(7)	0.0181(12)	0.3160(5)	0.221(1)	0.24(19)
$\mathrm{Sr2_a}$	4*b*	0.7514(7)	0.0181(12)	0.3160(5)	0.066	0.24(19)
$\mathrm{Ca2_a}$	4*b*	0.7514(7)	0.0181(12)	0.3160(5)	0.727(1)	0.24(19)
$\mathrm{Pr2_b}$	4*b*	0.7439(7)	0.5046(12)	0.8177(5)	0.221(1)	0.21(18)
$\mathrm{Sr2_b}$	4*b*	0.7439(7)	0.5046(12)	0.8177(5)	0.066	0.21(18)
$\mathrm{Ca2_b}$	4*b*	0.7439(7)	0.5046(12)	0.8177(5)	0.727(1)	0.21(18)
$\mathrm{Pr2_c}$	4*b*	0.037(2)	0.0020(9)	0.8155(3)	0.221(1)	0.24(14)
$\mathrm{Sr2_c}$	4*b*	0.037(2)	0.0020(9)	0.8155(3)	0.066	0.24(14)
$\mathrm{Ca2_c}$	4*b*	0.037(2)	0.0020(9)	0.8155(3)	0.727(1)	0.24(14)
$\mathrm{Pr2_d}$	4*b*	0.5037(2)	−0.0247(9)	0.8155(3)	0.221(1)	0.05(12)
$\mathrm{Sr2_d}$	4*b*	0.5037(2)	−0.0247(9)	0.8155(3)	0.066	0.05(12)
$\mathrm{Ca2_d}$	4*b*	0.5037(2)	−0.0247(9)	0.8155(3)	0.727(1)	0.05(12)
Mn1	4*b*	0.7502(10)	0.0067(16)	0.0990(4)	1	0.11(9)
Mn1′	4*b*	0.7540(10)	0.5067(16)	0.5990(4)	1	0.11(9)
Mn2	4*b*	0.0019(5)	0.0162(17)	0.6008(5)	1	0.01(8)
Mn2′	4*b*	0.5019(5)	−0.0108(17)	0.5994(5)	1	0.01(8)
$\mathrm{O1_a}$	2*a*	0.743(2)	0.104(6)	0.0	1	0.11(19)
$\mathrm{O1_b}$	2*a*	0.278(4)	0.049(6)	0.0	1	0.11(19)
$\mathrm{O1_c}$	2*a*	−0.017(4)	0.469(4)	0.0	1	0.11(19)
$\mathrm{O1_d}$	2*a*	0.496(4)	0.469(4)	0.0	1	0.11(19)
$\mathrm{O2_a}$	4*b*	0.750(3)	−0.042(6)	0.1992(19)	1	0.50(14)
$\mathrm{O2_b}$	4*b*	0.775(3)	0.497(6)	0.6948(19)	1	0.50(14)
$\mathrm{O2_c}$	4*b*	−0.007(3)	0.054(5)	0.6973(19)	1	0.50(14)
$\mathrm{O2_d}$	4*b*	0.502(3)	0.054(5)	0.7007(19)	1	0.50(14)
$\mathrm{O3_a}$	4*b*	0.868(2)	0.272(4)	0.1093(16)	1	0.54(12)
$\mathrm{O3_b}$	4*b*	0.870(2)	0.768(4)	0.5936(16)	1	0.54(12)
$\mathrm{O3_c}$	4*b*	0.114(2)	0.265(4)	0.5917(16)	1	0.54(12)
$\mathrm{O3_d}$	4*b*	0.116(2)	0.761(4)	0.0748(16)	1	0.54(12)
$\mathrm{O3_e}$	4*b*	0.367(2)	0.237(4)	0.1129(16)	1	0.54(12)
$\mathrm{O3_f}$	4*b*	0.369(2)	0.733(4)	0.6022(16)	1	0.54(12)
$\mathrm{O3_g}$	4*b*	0.613(2)	0.230(4)	0.5905(16)	1	0.54(12)
$\mathrm{O3_h}$	4*b*	0.615(2)	0.726(4)	0.0880(16)	1	0.54(12)

individual modes. The obtained results are summarized in Table VI, and the fit can be consulted in the Supplemental Material [38]. The checkerboard pattern is preserved in the CO3 phase, even though there are four nonequivalent sites for Mn atoms. The charge segregation between Mn1 (or Mn1′) and Mn2 (or Mn2′) is like the one observed for CO2 and CO1 phases. All $\mathrm{MnO_6}$ octahedra are quite anisotropic in the CO3 phase as well as on the other phases, and in the case of Mn1 (and Mn1′), there is still a small Jahn-Teller-like distortion with increased amplitude. However, this rise must be taken with caution because the determination of atomic coordinates has a lower precision in these measurements using the MAD detector (compare Tables V and VI). The preservation of this distortion below T_{S} agrees with the small changes observed in the resonant scattering of some diffraction peaks ascribed to the OO [35].

IV. CONCLUSIONS

Three different CO phase transitions have been identified and fully characterized in $\mathrm{Pr(Sr_{0.1}Ca_{0.9})_2Mn_2O_7}$ using the SXRPD technique. The mode decomposition analysis has allowed us to determine the structural changes associated with each transition with respect to the ideal undistorted tetragonal structure (*I*4/*mmm*). The high-temperature phase (charge disordered) exhibits orthorhombic symmetry (*Amam*) due to cooperative $a^-a^-c^0$ tilts of the $\mathrm{MnO_6}$ octahedra (irrep X3−). On cooling, the condensation of secondary modes, mainly belonging to the irreps DT2 and X1+, leads to a split of Mn atoms into two nonequivalent sites (Mn1 and Mn2) forming a checkerboard arrangement in the perovskite bilayers, giving rise to the CO1 phase. A Jahn-Teller-like distortion of the basal oxygens (irrep DT2) produces an anisotropic distortion for the octahedron base of $\mathrm{Mn1O_6}$, arranged in zigzag chains along the *b* direction (see Fig. 6). This configuration is responsible for the doubling of the *b* axis and the so-called OO reflections. The breathing mode (irrep X1+) is responsible for a small charge difference between Mn1 and Mn2 crystal sites. The resulting structure is centrosymmetric (*Pbnm*) with secondary antiferrodistortive distortions associated with irrep M5− parallel to the *b* axis. At lower temperature, the CO2 phase is characterized by a relative direction change between the modes of irreps DT2 and X3−. This direction change leads to a different orientation of the zigzag chains that now produces the doubling of the *a* axis. The simultaneous condensation of DT1 modes splits the Mn2 site (Mn2 and Mn2′), giving rise to three nonequivalent sites for Mn atoms but with a similar charge segregation between Mn1 and Mn2 sites. This direction change suppresses the activation of antiferrodistortive modes from irrep M5− and favors the condensation of ferrodistortive GM5− modes along the *b* axis, resulting in a polar structure with *Am*2*m* symmetry. This appealing phase is finally substituted by a more complex—also polar—ground state or CO3 phase, resulting from another direction change of the irrep X3−. This transition has two important consequences. Firstly, the Mn1 is split (Mn1 and Mn1′), and now there are four nonequivalent Mn sites, but both the checkerboard order and the charge segregation are preserved. Secondly, the primary distortion mode is now a coupled tilt of $\mathrm{MnO_6}$ octahedra following the $a^-b^-c^0$ tilt system that is also modulated by DT1 and DT2 modes. The $a^0\,b^0\,c^+$ rotation is active but minority in this distortion. Anyway, all $\mathrm{MnO_6}$ octahedra adopt the $a^-b^-c^+$ tilt schema in the ground state, and the CO2 phase could be considered an intermediate phase between CO1 and CO3. This point shows that the distorted structures present in this compound are mainly determined by the direction of the MnO_6 tilts [44].

Summarizing, this paper nicely illustrates that the relative directions of the two main nonpolar distortions (irreps X3− and DT2) participating in a trilinear coupling mechanism are key for the condensation of a secondary ferroelectric distortion (following the irrep GM5−). It is noteworthy that this kind of trilinear coupling is related to but different from the improper hybrid mechanism reported previously for related phases [23,41], and this finding widens the playground to look for improper ferroelectrics in perovskite-based structures.

ACKNOWLEDGMENTS

The authors would like to acknowledge the use of Servicio General de Apoyo a la Investigación-SAI, Universidad de Zaragoza. Granted beam time at ALBA synchrotron is appreciated (Proposal No. 2018093038). For financial support, we thank the Spanish Ministerio de Ciencia, Innovación y Universidades (Projects No. PID2021-124734OB-C21 and No. PID2021-124734OB-C22 cofunded by ERDF from EU, and Severo Ochoa FUNFUTURE, CEX2019-000917-S), Gobierno de Aragón (Project No. E12-23R), and Generalitat de Catalunya (Project No. 2021 SGR 00445).

[1] J. M. D. Coey, M. Viret, and S. von Molnár, Mixed-valence manganites, Adv. Phy **48**, 167 (1999).

[2] Y. Tokura, Critical features of colossal magnetoresistive manganites, Rep. Prog. Phys. **69**, 797 (2006).

[3] L. P. Gor'kov and V. Z. Kresin, Mixed-valence manganites: Fundamentals and main properties, Phys. Rep. **400**, 149 (2004).

[4] P. Radaelli, D. Cox, and M. Marezio, Charge, orbital, and magnetic ordering in $La_{0.5}Ca_{0.5}MnO_3$, Phys. Rev. B **55**, 3015 (1997).

[5] S. Mori, C. H. Chen, and S.-W. Cheong, Pairing of charge-ordered stripes in $(La, Ca)MnO_3$, Nature (London) **392**, 473 (1998).

[6] Y. Murakami, H. Kawada, H. Kawata, M. Tanaka, T. Arima, Y. Moritomo, and Y. Tokura, Direct observation of charge and orbital ordering in $La_{0.5}Sr_{1.5}MnO_4$, Phys. Rev. Lett. **80**, 1932 (1998).

[7] Y. Tokunaga, T. Lottermoser, Y. Lee, R. Kumai, M. Uchida, T. Arima, and Y. Tokura, Rotation of orbital stripes and the consequent charge-polarized state in bilayer manganites, Nat. Mater. **5**, 937 (2006).

[8] Y. Tokunaga, T. J. Sato, M. Uchida, R. Kumai, Y. Matsui, T. Arima, and Y. Tokura, Versatile and competing spin-charge-orbital orders in the bilayered manganite system $Pr(Sr_{1-y}Cay)_2Mn_2O_7$, Phys. Rev. B **77**, 064428 (2008).

[9] E. O. Wollan and W. C. Koehler, Neutron diffraction study of the magnetic properties of the series of perovskite-type compounds $[(1-x)La,\ xCa]MnO_3$, Phys. Rev. **100**, 545 (1955).

[10] J. Herrero-Martín, J. García, G. Subías, J. Blasco, and M. C. Sánchez, Structural origin of dipole x-ray resonant scattering in the low-temperature phase of $Nd_{0.5}Sr_{0.5}MnO_3$, Phys. Rev. B **70**, 024408 (2004).

[11] J. García, J. Herrero-Martín, G. Subías, J. Blasco, J. S. Andreu, and M. C. Sánchez, Incommensurate sinusoidal oxygen modulations in layered manganites $La_{1-x}Sr_{1+x}MnO_4$ ($x \geqslant 0.5$), Phys. Rev. Lett. **109**, 107202 (2012).

[12] G. Giovannetti, S. Kumar, J. van den Brink, and S. Picozzi, Magnetically induced electronic ferroelectricity in half-doped manganites, Phys. Rev. Lett. **103**, 037601 (2009).

[13] K. F. Wang, J. M. Liu, and Z. F. Ren, Multiferroicity: The coupling between magnetic and polarization orders, Adv. Phys. **58**, 321 (2009).

[14] D. Okuyama, Y. Tokunaga, R. Kumai, Y. Taguchi, T. Arima, and Y. Tokura, Lattice-form-dependent orbital shape and charge disproportionation in charge- and orbital-ordered manganites, Phys. Rev. B **80**, 064402 (2009).

[15] Y. Tokunaga, R. Kumai, N. Takeshita, Y. Kaneko, J. P. He, T. Arima, and Y. Tokura, Effects of uniaxial stress on orbital stripe direction in half-doped layered manganites: $Eu_{0.5}Ca_{1.5}MnO_4$ and $Pr(Sr, Ca)_2Mn_2O_7$, Phys. Rev. B **78**, 155105 (2008).

[16] R. Thiyagarajan, G. Deng, S. Arumugam, D. Mohan Radheep, U. Devarajan, A. Murugeswari, P. Mandal, E. Pomjakushina, and K. Conder, Effect of magnetic field and pressure on charge-orbital ordering in $Pr(Sr_{1-x}Ca_x)_2Mn_2O_7$ ($x = 0.4$ and 0.9) single crystals, J. Appl. Phys. **110**, 093905 (2011).

[17] Z. He, H. Tian, G. Deng, Q. Xu, and G. Van Tendeloo, Microstructure of bilayer manganite $PrCa_2Mn_2O_7$ showing charge/orbital ordering, Appl. Phys. Lett. **102**, 212902 (2013).

[18] Z. B. He, G. Deng, H. Tian, Q. Xu, and G. Van Tendeloo, 90 ° rotation of orbital stripes in bilayer manganite $PrCa_2Mn_2O_7$ studied by *in situ* transmission electron microscopy, J. Solid State Chem. **200**, 287 (2013).

[19] C. Ma, Y. Lin, H. Yang, H. Tian, L. Shi, J. Zeng, and J. Li, Direct observation of magnetic-ion off-centering-induced ferroelectricity in multiferroic manganite $Pr(Sr_{0.1}Ca_{0.9})_2Mn_2O_7$, Adv. Mater. **27**, 6328 (2015).

[20] S. Lafuerza, J. García, G. Subías, J. Blasco, K. Conder, and E. Pomjakushina, Intrinsic electrical properties of $LuFe_2O_4$, Phys. Rev. B **88**, 085130 (2013).

[21] K. Yamauchi and S. Picozzi, Mechanism of ferroelectricity in half-doped manganites with pseudocubic and bilayer structure, J. Phys. Soc. Jpn. **82**, 113703 (2013).

[22] A. M. Glazer, Simple ways of determining perovskite structures, Acta Cryst. A **31**, 756 (1975).

[23] N. A. Benedek, J. M. Rondinelli, H. Djani, P. Ghosez, and P. Lightfoot, Understanding ferroelectricity in layered perovskites: New ideas and insights from theory and experiments, Dalt. Trans. **44**, 10543 (2015).

[24] J. Blasco, G. Subías, J. L. García-Muñoz, F. Fauth, M. C. Sánchez, and J. Garciá, Symmetry mode analysis of distorted polar/nonpolar structures in A-site ordered $SmBaMn_2O_6$ perovskite, Phys. Rev. B **103**, 214110 (2021).

[25] J. Blasco, M. C. Sánchez, J. García, J. Stankiewicz, and J. Herrero-Martín, Growth of $Sr_{2/3}Ln_{1/3}FeO_3$ ($Ln =$ La, Pr, and Nd) single crystals by the floating zone technique, J. Cryst. Growth **310**, 3247 (2008).

[26] J. Rodríguez-Carvajal, Recent advances in magnetic structure determination by neutron powder diffraction, Physica B: Condens. Matter **192**, 55 (1993).

[27] B. J. Campbell, J. S. O. Evans, F. Perselli, and H. T. Stokes, Rietveld Refinement of structural

distortion-mode amplitudes, IUCr Comput. Comm. Newsl. **8**, 81 (2007).

[28] J. M. Perez-Mato, D. Orobengoa, and M. I. Aroyo, Mode crystallography of distorted structures, Acta Cryst. A **66**, 558 (2010).

[29] B. J. Campbell, H. T. Stokes, D. E. Tanner, and D. M. Hatch, ISODISPLACE: A web-based tool for exploring structural distortions, J. Appl. Crystallogr. **39**, 607 (2006).

[30] K. Momma and F. Izumi, VESTA 3 for three-dimensional visualization of crystal, volumetric and morphology data, J. Appl. Crystallogr. **44**, 1272 (2011).

[31] F. Fauth, I. Peral, C. Popescu, and M. Knapp, The new material science powder diffraction beamline at ALBA Synchrotron, Powder Diffr. **28**, S360 (2013).

[32] J. Blasco, J. A. Rodríguez-Velamazán, J. L. García-Muñoz, V. Cuartero, S. Lafuerza, and G. Subías, Structural and magnetic properties of $Ca_3Mn_{2-x}Ru_xO_7$ ($0 < x \leqslant 0.9$), Phys. Rev. B **106**, 134403 (2022).

[33] I. D. Fawcett, E. Kim, M. Greenblatt, M. Croft, and L. A. Bendersky, Properties of the electron-doped layered manganates $La_{2-2x}Ca_{1+2x}Mn_2O_7$ ($0.6 \leqslant x \leqslant 1.0$), Phys. Rev. B **62**, 6485 (2000).

[34] G. Deng, R. Thiyagarajan, D. Mohan Radheep, E. Pomjakushina, M. Medarde, A. Krzton-Maziopa, S. Wang, S. Arumugam, and K. Conder, Floating zone crystal growth and magnetic properties of bilayer manganites $Pr(Sr_{1-x}Ca_x)_2Mn_2O_7$, J. Cryst. Growth **353**, 25 (2012).

[35] T. A. W. Beale, S. R. Bland, R. D. Johnson, P. D. Hatton, J. C. Cezar, S. S. Dhesi, M. V. Zimmermann, D. Prabhakaran, and A. T. Boothroyd, Thermally induced rotation of 3*d* orbital stripes in $Pr(Sr_{0.1}Ca_{0.9})_2Mn_2O_7$, Phys. Rev. B **79**, 054433 (2009).

[36] H. Itoh, Y. Tokunaga, N. Kida, R. Shimano, and Y. Tokura, Charge-ordering-induced polar domains and domain walls in a bilayered manganite $Pr(Sr_{0.15}Ca_{0.85})_2Mn_2O_7$, Appl. Phys. Lett. **96**, 032902 (2010).

[37] Z. A. Li, X. Li, Z. Wang, H. F. Tian, C. Ma, L. J. Zeng, and H. X. Yang, A “checkerboard” orbital-stripe phase and charge ordering transitions in $Pr(Sr_xCa_{2-x})Mn_2O_7$ ($0 \leqslant x \leqslant 0.45$), Epl **86**, 67010 (2009).

[38] See Supplemental Material at http://link.aps.org/supplemental/10.1103/PhysRevB.109.024111 for details about diffraction refinements with Rietveld plots and comparison of mode decomposition and atom shifts for different irreps.

[39] M. J. Pitcher, P. Mandal, M. S. Dyer, J. Alaria, P. Borisov, H. Niu, J. B. Claridge, and M. J. Rosseinsky, Tilt engineering of spontaneous polarization and magnetization above 300 K in a bulk layered perovskite, Science **347**, 420 (2015).

[40] I. D. Brown and D. Altermatt, Bond-valence parameters obtained from a systematic analysis of the inorganic crystal structure database, Acta Cryst. B **41**, 244 (1985).

[41] I. Etxebarria, J. M. Perez-Mato, and P. Boullay, The role of trilinear couplings in the phase transitions of Aurivillius compounds, Ferroeelctrics **401**, 17 (2010).

[42] J. Blasco, G. Subías, J. L. García-Muñoz, F. Fauth, and J. García, Determination of the crystal structures in the A-site-ordered $YBaMn_2O_6$ perovskite, J. Phys. Chem. C **125**, 19467 (2021).

[43] K. S. Aleksandrov and J. Bartolome, Octahedral tilt phases in perovskite-like crystals with slabs containing an even number of octahedral layers, J. Phys. Condens. Matter **6**, 8219 (1994).

[44] An alternative way to describe these successive transitions is obtained when using a different set of basis vectors (inverting **a** and **b** vectors in CO1, rotating 90° **a** and **b** in CO2 and CO3, with respect to the basis previously described). Then the transformations are described as three successive direction changes of the irrep X3− (i.e., MnO_6 tilts and the condensation of associated modes), whereas no direction changes occur in distortion DT2. This alternative description gives the same relative coupling between irreps X3− and DT2 that is the relevant fact.